Effect of an MLT dependent electron loss rate on the magnetosphere-ionosphere coupling

Matina Gkioulidou,[1,2] Chih-Ping Wang,[1] Simon Wing,[2] Larry R. Lyons,[1] Richard A. Wolf,[3] and Tung-Shin Hsu[1]

Received 14 June 2012; revised 16 September 2012; accepted 10 October 2012; published 27 November 2012.

[1] As plasma sheet electrons drift earthward, they get scattered into the loss cone due to wave-particle interactions and the resulting precipitation produces auroral conductance. Realistic electron loss is thus important for modeling the magnetosphere - ionosphere (M-I) coupling and the degree of plasma sheet electron penetration into the inner magnetosphere. In order to evaluate the significance of electron loss, we used the Rice Convection Model (RCM) coupled with a force-balanced magnetic field to simulate plasma sheet transport under different electron loss rates and under self-consistent electric and magnetic field. We used different magnitudes of i) strong pitch angle diffusion everywhere electron loss rate (strong rate) and ii) a more realistic loss rate with its MLT dependence determined by wave activity (MLT rate). We found that electron pressure under the MLT rate is larger compared to the strong rate inside $L \sim 12$ R_E. The dawn-dusk asymmetry in the precipitating electron energy flux under the MLT rate, with much higher energy flux at dawn than at dusk, agrees better with statistical DMSP observations. High-energy electrons inside $L \sim 8$ R_E can remain there for many hours under the MLT rate, while those under the strong rate get lost within minutes. Under the MLT rate, the remaining electrons cause higher conductance at lower latitudes; thus after a convection enhancement, the shielding of the convection electric field is less efficient, and as a result, the ion plasma sheet penetrates further earthward into the inner magnetosphere than under the strong rate.

Citation: Gkioulidou, M., C.-P. Wang, S. Wing, L. R. Lyons, R. A. Wolf, and T.-S. Hsu (2012), Effect of an MLT dependent electron loss rate on the magnetosphere-ionosphere coupling, *J. Geophys. Res.*, *117*, A11218, doi:10.1029/2012JA018032.

1. Introduction

[2] The electrons in the plasma sheet constantly undergo pitch angle scattering through wave-particle interactions and precipitate into the ionosphere. The precipitating electrons are the main contributors to ionospheric conductance within the nightside auroral oval, the conductance being a very important element of magnetosphere - ionosphere (M-I) coupling. More specifically, the spatial distribution of electron precipitation substantially affects the distribution of conductance, and as a result, the spatial distribution of the convection electric field [e.g., *Ebihara and Fok*, 2004; *Gkioulidou et al.*, 2009]. The convection electric field, in turn, determines the earthward penetration of both the lower energy electrons that contribute to the aurora, as well as the higher-energy electrons that become the seed population for radiation belt electrons [*Thorne et al.*, 2007]. Furthermore, the precipitation also results in loss of electrons from the plasma sheet, thus decreasing the number of electrons transported to the inner magnetosphere. Therefore, a realistic electron loss is crucial to modeling the electron population in the inner magnetosphere.

[3] The pitch angle scattering can be due to either electrostatic cyclotron harmonic (ECH) waves [*Kennel et al.*, 1970; *Kennel and Ashour-Abdalla*, 1982; *Ashour-Abdalla and Kennel*, 1978; *Lyons*, 1974, *Ni et al.*, 2011a] or whistler mode waves [*Johnstone et al.*, 1993; *Meredith et al.*, 1999; *Ni et al.*, 2011b]. *Chen and Schulz* [2001] established a magnetic local time (MLT) dependent scattering rate model (hereafter referred to as the Chen rate) based on statistical observations of 0.1–5 kHz frequency waves, which includes both ECH and whistler mode emissions [*Koons and Roeder*, 1990]. The observations show wave activity peaking toward dawn. Simulating bounce-averaged drifts of electrons and their losses by using the Chen rates, they obtained precipitating energy fluxes and conductivities that agreed better with statistical studies [*Hardy et al.*, 1985, 1987] than using strong diffusion everywhere loss rates. They also found better agreement between their modeled precipitating energy fluxes and PIXIE (Polar Ionospheric X-ray Imaging Experiment) data from a single storm event

[1]Department of Atmospheric and Oceanic Sciences, University of California, Los Angeles, California, USA.
[2]The Johns Hopkins University Applied Physics Laboratory, Laurel, Maryland, USA.
[3]Physics and Astronomy Department, Rice University, Houston, Texas, USA.

Corresponding author: M. Gkioulidou, The Johns Hopkins University Applied Physics Laboratory, 11101 Johns Hopkins Rd., Laurel, MD 21230, USA. (malamati.gkioulidou@jhuapl.edu)

0148-0227/12/2012JA018032

[*Anderson et al.*, 2000]. Although the Chen rate model is fairly simple, it is one step closer to more realistic loss rate modeling. However, the electric and magnetic field used in their simulations was not self-consistent, so the effect of the electron loss on the M-I coupling and transport of electrons into the inner magnetosphere could not be appropriately evaluated. Recently, *Ni et al.* [2011a, 2011b] have modeled loss rates, evaluating the contribution of both whistler mode chorus and ECH waves and taking into account the observed dependence of wave activity on geomagnetic activity. However, their results are limited in radial distance (L = 6) and MLT (0000–0600). Thus no other global loss rate models have become available yet that are more realistic than the Chen rate model.

[4] Therefore in this study, we investigate the effect of the Chen loss rate, in comparison with strong diffusion loss rate, on the ion and electron plasma sheet, their coupling with the ionosphere, and their penetration into the inner magnetosphere. We do this by modeling these processes under self-consistent electric and magnetic fields with the Rice Convection Model (RCM) combined with a modified Dungey force-balanced magnetic field solver. The MLT-dependent tail ion and electron sources are established based on statistical Geotail observations. In sections 4.1 and 4.2, we conduct different simulation runs with the Chen rate, strong diffusion rate, and fractions of the two rates for conditions of substorm growth phase and evaluate their resulting precipitating electron energy fluxes against statistical DMSP electron energy fluxes that were obtained also during the growth phase. We focus on the substorm growth phase only because the RCM cannot appropriately simulate non-adiabatic processes during the substorm expansion phase. We also compare the equatorial electron differential fluxes with statistical THEMIS electron energy spectra. In both the ionosphere and the equatorial plane, the simulations using Chen rates are found to account better for the observations. After establishing that there is better agreement between observations and simulation results using the more realistic Chen rate, in section 4.3, we evaluate how the M-I coupling under different loss rates affects the development of the shielding of the penetration electric field in the inner magnetosphere. For this part of the study we choose storm-like convection enhancement, which is stronger than the substorm growth phase, so that shielding and its effects on the earthward penetration of the plasma sheet can be seen more clearly. We find that the shielding under the Chen rate in the inner magnetosphere is less efficient, allowing deeper penetration of the plasma sheet.

2. Model

2.1. RCM Combined With Modified Dungey Force-Balanced Magnetic Field Solver

[5] The RCM [*Toffoletto et al.*, 2003] combined with a modified Dungey force-balanced magnetic field solver [*Gkioulidou et al.*, 2011] calculates the bounce–averaged electric and magnetic drift of ions and electrons assuming isotropic distributions along the magnetic field lines and a slow flow approximation, within self-consistently computed electric and magnetic fields.

[6] The self-consistent electric field is obtained by satisfying current continuity both in the magnetosphere and ionosphere via field-aligned currents [*Vasyliunas*, 1970], namely

$$\nabla \cdot [\Sigma \cdot (\nabla \Phi_i)] = -j_{\parallel} \sin(I) = -\frac{B_i}{2B} \hat{b} \cdot \nabla V \times \nabla p \sin(I) \quad (1)$$

where Σ is the field-line integrated conductivity tensor, Φ is the electric potential, I is the dip angle of the magnetic field in the ionosphere, and $j_{\parallel}$ is the ionospheric field-aligned current density of the northern or southern hemisphere (north-south symmetry is assumed), V and p are flux tube volume per unit magnetic flux and pressure respectively at the equatorial plane, and B is the magnetic field. Index i refers to ionosphere-computed quantities. With given Σ and boundary conditions at the high and low-latitude boundary, (1) can be solved to obtain the electric potential Φ_i. The conductance tensor Σ includes both the Hall and Pedersen conductances. The conductivity includes Solar-EUV-generated conductivity that is estimated from the IRI-90 empirical ionosphere driven by F10.7 and the Ap index, and auroral conductance, which is discussed in detail in section 2.4. The high-latitude boundary condition for the potential is a Dirichlet boundary condition; the overall strength of convection is determined by setting the total range of potential on the boundary equal to the polar-cap potential drop $\Delta\Phi_{PC}$. A two-cell convection pattern is assigned to describe the electric potential inside the polar cap. As for the low-latitude boundary, we neglect neutral winds and apply the standard RCM boundary condition [*Toffoletto et al.*, 2003] at 45 degrees latitude. Placed at that location, the boundary condition provides only a crude representation of the effect of the equatorial electrojet, but the matter is of little consequence for results above 60 degrees latitude, which are the focus of this paper.

[7] Force-balance with RCM plasma pressures in the equatorial plane is obtained using the modified Dungey force-balanced magnetic field solver [*Liu et al.*, 2006; *Schulz and Chen*, 2008; *Gkioulidou et al.*, 2011]. The original current-free Dungey model [*Dungey*, 1963] assumes a dipolar **B** field plus a uniform "southward" perturbation $\Delta\mathbf{B}$ parallel to the magnetic dipole axis. The modified Dungey solver, by expressing the magnetic field with Euler potentials, allows the magnetic field line stretching to vary with MLT and radial distance in accordance with equatorial pressure profiles and allows the fields to be numerically computed rather efficiently. However, our magnetic field model has certain limitations: (i) the force balance is calculated only in the equatorial plane, so that balance in the off-equatorial region is not achieved perfectly, resulting in limited field line stretching; and (ii) each magnetic field line lies in a meridian plane, so that azimuthal perturbations of the magnetic field cannot be accounted for. For more details regarding the coupled model, see *Gkioulidou et al.* [2011].

2.2. RCM Electron Loss

[8] The RCM treats particle drifts under the assumption of strong, elastic pitch angle scattering. Particles of the same energy invariant λ_k in eV·$(R_E/nT)^{2/3}$ ($\lambda_k = E_k \cdot V^{2/3}$, where k is an index for energy channel and E_k is particle kinetic energy in eV and V is the flux tube volume in R_E/nT) move along the electric and magnetic drift paths so the total energy $q\Phi + \lambda_k \cdot V^{-2/3}$ is conserved for time-independent electric

and magnetic fields, where q is electric charge (+1 for protons and −1 for electrons). The number of particles of energy invariant λ_k within the energy range from $\lambda_{k,\min}$ to $\lambda_{k,\max}$ and within V is defined as particle number content η_k ($\eta_k = 4\pi \cdot 2^{1/2} m^{3/2} \cdot \int |\lambda|^{1/2} \cdot f_k(\lambda) d\lambda$, where the integral is over the λ-range covered by energy channel k, m is the particle's mass, and f is phase space density, so that $\eta_k = n_k \cdot V$, where n_k is partial number density within the energy channel). η_k is conserved along these particles' drift paths unless there are local particle losses that remove existing particles or local particle sources that add new particles. In the RCM, electron loss due to precipitation is modeled by

$$\eta_k(\mathbf{x}, t) = \eta_k(\mathbf{x} - \mathbf{v}dt, t - dt) e^{-dt * loss\,rate} \tag{2}$$

where $\mathbf{x}$ is the position and $\mathbf{v}$ the drift speed. The loss rate used in our simulations will be discussed in more detail in section 3.1.

2.3. Electron Precipitation

[9] Electrons that get lost from the plasma sheet precipitate into the ionosphere. The electron precipitating energy flux Φ_E in erg cm^{-2} s^{-1} is expressed by

$$\Phi_E = \pi \sum_k E_k J(E_k) dE \tag{3}$$

where dE is the width of the energy channel, and $J(E_k)$ is the precipitating electron differential flux in sr^{-1} eV^{-1} cm^{-2} s^{-1} given by

$$J(E_k) = 7.39 \cdot 10^{-16} \frac{\sqrt{\lambda_k} \eta_{k(precipitating)} V^{-2/3}}{\frac{\lambda_{k+1} - \lambda_{k-1}}{2}} \tag{4}$$

$\eta_{k(precipitating)}$ in equation (4) is the flux tube volume electron content within the loss cone and it depends on the η_k outside the loss cone and the electron loss rate,

$$\eta_{k(precipitating)} = factor * \eta_k \tag{5}$$

where,

$$factor = \frac{loss\,rate}{strong\ diffusion\ loss\,rate} \tag{6}$$

The strong diffusion loss rate is the maximum precipitation loss rate for the case of zero field-aligned potential drop and is expressed by

$$1/\tau = \sqrt{\frac{E_k}{2m}} \frac{1}{B_i} \frac{1}{V} \tag{7}$$

where B_i is the ionospheric magnetic field and m is the electron mass. Note that in our calculation of strong diffusion loss rate we do not include the backscatter coefficient that would account for electrons that mirror at or below the altitude of 0.02 R_E and are scattered back to the flux tube instead of precipitating into the atmosphere.

2.4. Auroral Conductance

[10] The RCM auroral height-integrated Pedersen and Hall conductivities are estimated by the electron precipitation from the simulated plasma distributions, using the algorithms of *Robinson et al.* [1987], namely

$$\Sigma_P = \frac{40\langle E \rangle}{16 + \langle E \rangle^2} \Phi_E^{1/2} \tag{8}$$

$$\frac{\Sigma_H}{\Sigma_p} = 0.45 \langle E \rangle^{0.85} \tag{9}$$

where Σ_P and Σ_H are the height-integrated Pedersen and Hall conductivities respectively in ohms^{-1}, Φ_E is the precipitating energy flux given by (3), and $\langle E \rangle$ is the average energy in keV expressed by

$$\langle E \rangle = \frac{\sum_k E_k J(E_k) dE}{\sum_k J(E_k) dE} \tag{10}$$

where $J(E_k)$ is the precipitating electron differential flux given by (4). The relation between average energy and conductance is derived assuming a Maxwellian electron energy distribution. Our electron distribution at the RCM boundary covers the majority of plasma sheet electrons from few eV to hundreds of keV, a range sufficiently large for computing accurate ⟨E⟩ using equation (10) and conductance using equations (8) and (9). However, in our conductance calculations we have excluded the electron population with energies below 500 eV, as suggested by *Robinson et al.* [1987]. That is because, although the fluxes for these low auroral electron energies are considerably higher than those given by a Maxwellian distribution, their contribution to height-integrated conductance is very small since they deposit their energy at altitudes where the collision frequency is too low to sustain currents perpendicular to the magnetic field.

3. Simulation Setup

[11] We investigate how the electron loss rate affects the electron precipitation to the ionosphere, and we determine which electron loss rate can better account for the precipitating electron energy fluxes observed by DMSP. Since the statistical DMSP results used for the comparisons were obtained during the substorm growth phase, we established our simulation conditions for the solar wind driving and tail particle sources based on observations also during substorm growth phase.

3.1. Electron Loss Rates

[12] We focus on the effect of different electron loss rates on the auroral conductance, and through that on the convection electric field and the resulting penetration of the plasma sheet into the inner magnetosphere. We have conducted runs using six different scattering rates, which can be divided into two groups. The first group assumes the strong diffusion loss rate given by (6) everywhere and 2/3 and 1/3 of that rate, while the second group assumes the MLT dependent Chen rate and 2/3, and 1/3 of that rate. The magnitude and spatial distribution of waves vary with geomagnetic activity, but the Chen rate does not include this variability. The particular fractions chosen for both rates were motivated by the study of *Schumaker et al.* [1989],

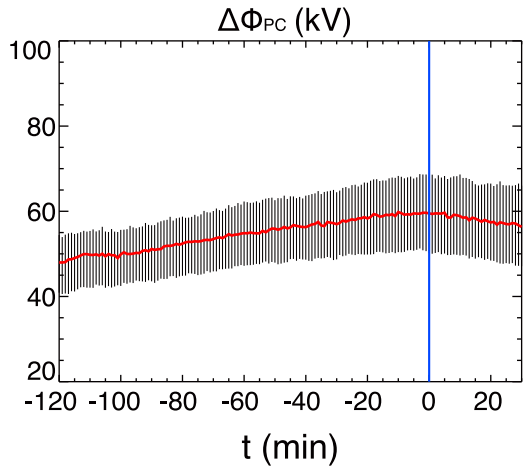

Figure 1. Statistical temporal variations of $\Delta\Phi_{PC}$, based on the *Weimer* [1995] model, during the substorm events of the *Hsu and McPherron* [2012] substorm list. The red line is the median value, while the vertical black lines indicate the 25% and 75% quartiles. The blue line indicates the substorm onset.

where data from near-geosynchronous SCATHA satellite in conjunction with polar-orbiting P78–1 revealed that the average lifetimes of plasma sheet electrons exceed those for the case of isotropy by a factor between 2 and 3 for $Kp \leq 2$ (between 1/2 and 1/3 of strong diffusion loss rate), and 1.5 for $Kp > 2$ (2/3 of strong diffusion loss rate).

[13] The main difference between the above two groups is that the spatial dependence of the loss rate under strong diffusion comes only from the spatial variability of the magnetic field and electron energy, while the Chen rate ρ_{MLT} also depends on the wave activity through the SCATHA wave occurrence frequency distribution [*Koons and Roeder*, 1990], and is given by

$$\rho_{MLT} = \rho(E_k, L)[1 + 0.8\sin(\varphi - \pi/4)] \tag{11}$$

where φ is the MLT coordinate (0 at midnight, $\pi/2$ at dawn, π at noon, and $3\pi/2$ at dusk) and

$$\rho(E_k, L) = \min\left[0.08E_k^{-1.32}, 0.4 \times 10^{(2L-6+0.4\log_2 E_k)}\right](day^{-1}) \tag{12}$$

is a less than everywhere strong scattering rate (energy E_k in MeV, and L is the dimensionless label of the magnetic shell), which is based on extrapolated theoretical lifetimes by *Albert* [1994] that have been renormalized to match the empirical lifetimes by *Roberts* [1969]. These empirical and theoretical estimates correspond to the limit of the weak pitch angle diffusion, for which the particle lifetime is inversely proportional to the scattering rate ρ. In the extrapolated regimes, especially where $1/\rho_{MLT}(E_k, L)$ is smaller than the corresponding lifetimes against strong diffusion τ, a simple model [*Schulz*, 1974] is used for the loss rate, leading to a smooth transition between weak pitch angle diffusion and strong diffusion, namely $\bar{\rho}_{MLT} = \rho_{MLT}/(1 + \rho_{MLT}\tau)$. The Chen rate, ρ_{MLT}, reaches a maximum at φ = 9 MLT, and a minimum at φ = 21 MLT according to wave activity.

[14] As shown later in this paper, under a more realistic loss rate, electrons become less isotropic with decreasing radial distances in the inner magnetosphere due to weakening of the pitch angle diffusion. However, the RCM still treats the drift of these electrons as being isotropic. Nevertheless, in this study we overlook this inconsistency.

3.2. Plasma Boundary and Initial Conditions

[15] The location of the outer boundary is specified as a 15 R_E circle centered at X = −5 R_E and Y = 0 in the equatorial plane, and reaches X = −20 R_E at midnight and |Y| = 15 R_E (on the dawn and dusk sides). The latitudes in the ionosphere that map to the outer boundary vary as the magnetic field changes. The inner boundary is at $r_0 \sim 2$ R_E. Along the outer boundary, the proton and electron distributions at different MLT are established from a fitting of two-component kappa distributions to statistical results of substorm growth phase periods observed by Geotail and THEMIS from 1996 to 2010. Substorm onsets were obtained from the list of *Hsu and McPherron* [2012] that is based on an appropriate change of AL. The data have been sorted into three time-ranges 120–60, 60–30, and 30–0 min before the substorm onset. Only isolated substorms, i.e., at least 3hr after the previous substorm, were used. The two-component kappa distribution is given by

$$f = N_c\left(\frac{m}{2\pi\kappa_c E_{0,c}}\right)^{3/2}\frac{\Gamma(\kappa_c+1)}{\Gamma(\kappa_c-1/2)}\left[1+\frac{E}{\kappa_c E_{0,c}}\right]^{-\kappa_c-1} + N_h\left(\frac{m}{2\pi\kappa_h E_{0,h}}\right)^{3/2}\frac{\Gamma(\kappa_h+1)}{\Gamma(\kappa_h-1/2)}\left[1+\frac{E}{\kappa_h E_{0,h}}\right]^{-\kappa_h-1} \tag{13}$$

where f is phase space density, N is density, m is particle mass, and κ and the energy of the peak particle flux E_0 are parameters of the kappa distribution (subscript c (h) is for cold (hot) population). N, κ, and E_0 are free parameters in the fitting [*Wang et al.*, 2007, 2011].

[16] For initial plasma conditions, we use plasma distributions obtained from our previous RCM run [*Wang et al.*, 2011], where we started with an empty magnetosphere and plasma from the tail boundary moved into the inner magnetosphere under many hours of enhanced convection. The boundary conditions and temporal variations of the polar cap potential drop of that run are shown in Figure 5 of *Wang et al.* [2011].

3.3. Simulation Runs

[17] For all the six simulation runs, we first started with the plasma sheet boundary conditions corresponding to 120–60 min before the substorm onset, and ran simulations with constant cross polar-cap potential drop ($\Delta\Phi_{PC}$) of 40 kV for 5 simulation hours. This allows particles from the tail boundary to populate regions of open drift paths, while particles that remain on the closed paths are from the initial conditions. We then gradually increased $\Delta\Phi_{PC}$ to 60 kV over two hours (t = 5–7 h). This specified $\Delta\Phi_{PC}$ change from 40 to 60 kV is determined from the statistical temporal variations of the $\Delta\Phi_{PC}$, based on the *Weimer* [1995] model, from the substorm events we used to establish our tail boundary conditions (see section 3.2). These variations are shown in Figure 1.

[18] The magnetic field was updated every 10 min to maintain force balance with the RCM pressures. We also

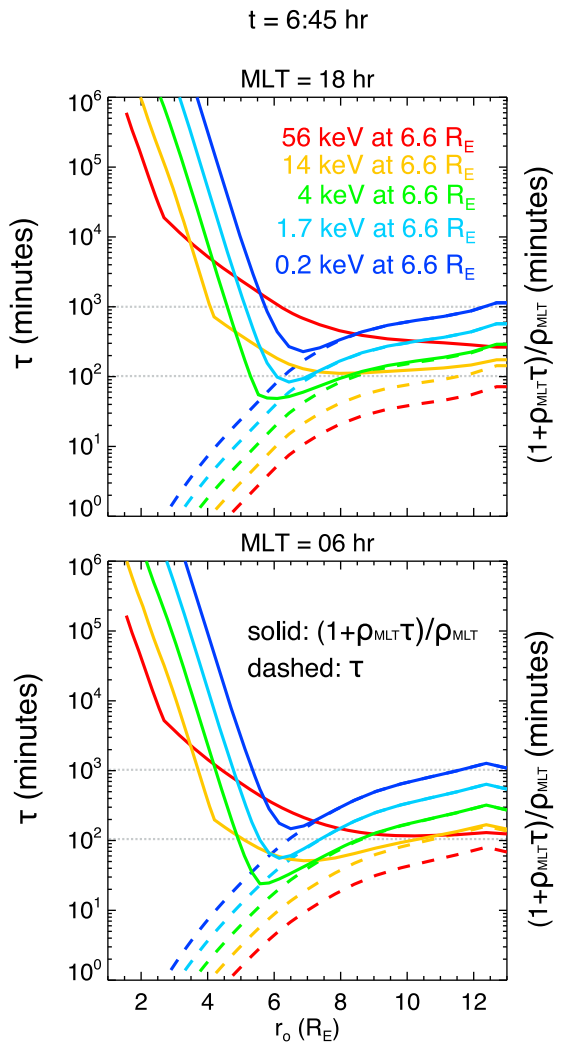

Figure 2. Radial profiles of lifetime τ against strong diffusion with dashed lines, and lifetime $1/\bar{\rho}_{MLT}$ with solid lines, for five different invariant energies corresponding to 56, 14, 4, 1.7, 0.2 keV at 6.6 R_E with red, yellow, green, light blue, and purple respectively, at (top) dusk and (bottom) dawn. The gray lines indicate 100 and 1000 min.

changed the plasma tail boundary conditions at t = 6:00 and 6:30 to those corresponding to 60–30 min, and 30–0 min before the onset respectively. In sections 4.1–4.2 below we discuss the results at t = 6:45 h, which represents 15 min before substorm onset.

4. Simulation Results

4.1. Effect of MLT Dependent Loss Rates on Plasma Sheet and Inner Magnetosphere Electrons

[19] We first investigate how different loss rates affect the electron population in the plasma sheet and inner magnetosphere. We thus examine the lifetimes of plasma sheet electrons of different energies resulting from strong diffusion loss rates everywhere, in comparison to the Chen rates. Figure 2 compares the radial profiles of lifetime τ under strong diffusion (dashed lines) and lifetime under the Chen rate, $1/\bar{\rho}_{MLT}$, (solid lines) for the five different invariant energies at 6.6 R_E identified in the figure at dusk (Figure 2, top) and dawn (Figure 2, bottom). It can be seen that, at both local times and for energies of 4 keV and below, the Chen lifetimes approach the limit of strong diffusion lifetimes at 7–12 R_E. However, the Chen lifetimes of the two higher energy channels (14 keV and 56 keV) barely reach the strong diffusion limit (especially at dusk where the Chen rates are weaker). For energies between 4 keV and 56 keV, the Chen lifetimes at dawn are significantly shorter than at dusk. For 2 $R_E \le r_0 \le 6$ R_E and for all energies, the Chen lifetimes become significantly larger than the strong diffusion ones with decreasing radial distance because they take into account weak particle diffusion in that region.

[20] With the same outer particle sources, the different loss rates result in quite different spatial distributions of the electron plasma sheet. In Figure 3 we show the electron pressures for the six different cases, with runs under the Chen rate and its fractions on the left, and runs under the strong diffusion rate and its fractions on the right. The bold dashed black circle in all plots indicates the geocentric radius of 8 R_E. As expected, for both the strong diffusion and Chen rates, electron pressure within 12 R_E decreases with increasing loss rates, that is, going from a to b and c or from d to e and f. Also these differences become larger with decreasing radial distances, since the numbers of electrons are the same at the outer boundary for these runs. The electron pressures of the strong diffusion everywhere cases are clearly lower than those of the Chen rate cases in the premidnight sector between 18–00 MLT and from $r_o \sim 8$ to $\sim$12 R_E. This is due to the Chen lifetimes for higher energy electrons being much larger than the strong diffusion everywhere lifetimes at dusk beyond 8 R_E, and it results in stronger dawn-dusk electron pressure asymmetry under strong diffusion everywhere. Finally, we note the significantly larger electron pressure inside 8 R_E for all the Chen rate cases, compared to the respective strong diffusion ones. This is due to the much weaker loss rates at smaller radial distances in the Chen rate cases, which allow the electrons trapped within the closed drift trajectories inside $\sim$7 R_E to remain there for much longer time.

[21] To further investigate this last point, Figure 4 shows the electron energy spectra at geosynchronous orbit at midnight (Figure 4, top), dusk (Figure 4, middle), and dawn (Figure 4, bottom), for strong diffusion rate cases (dashed lines) and for Chen rate cases (solid lines). We can see that, indeed, in the Chen rate cases, the differential flux of electrons of 10 keV and above is significantly increased in comparison with the strong diffusion everywhere cases especially at dusk where the Chen rate is weaker for high-energy electrons. We can also see the decrease in electron differential fluxes with increasing loss rate for both cases.

[22] Figure 5 shows the simulated electron energy spectra versus radial distance along the dawn meridian for the strong diffusion and Chen rate cases, and their comparison with the observed electron energy spectra taken from Figure 10 of *Wang et al.* [2011]. It is clear that, in addition to the nominal plasma sheet electrons of a few keV at $r_o > \sim$7 R_E, there is a distinctive population of energies from 20–200 keV inside $r_o \sim 8$ R_E in the Chen rate case that is not seen in the strong diffusion rate case. These are the electrons that penetrated further into the inner magnetosphere and remained there because of weak pitch angle scattering being included in the Chen loss rate. This high-energy electron population in the

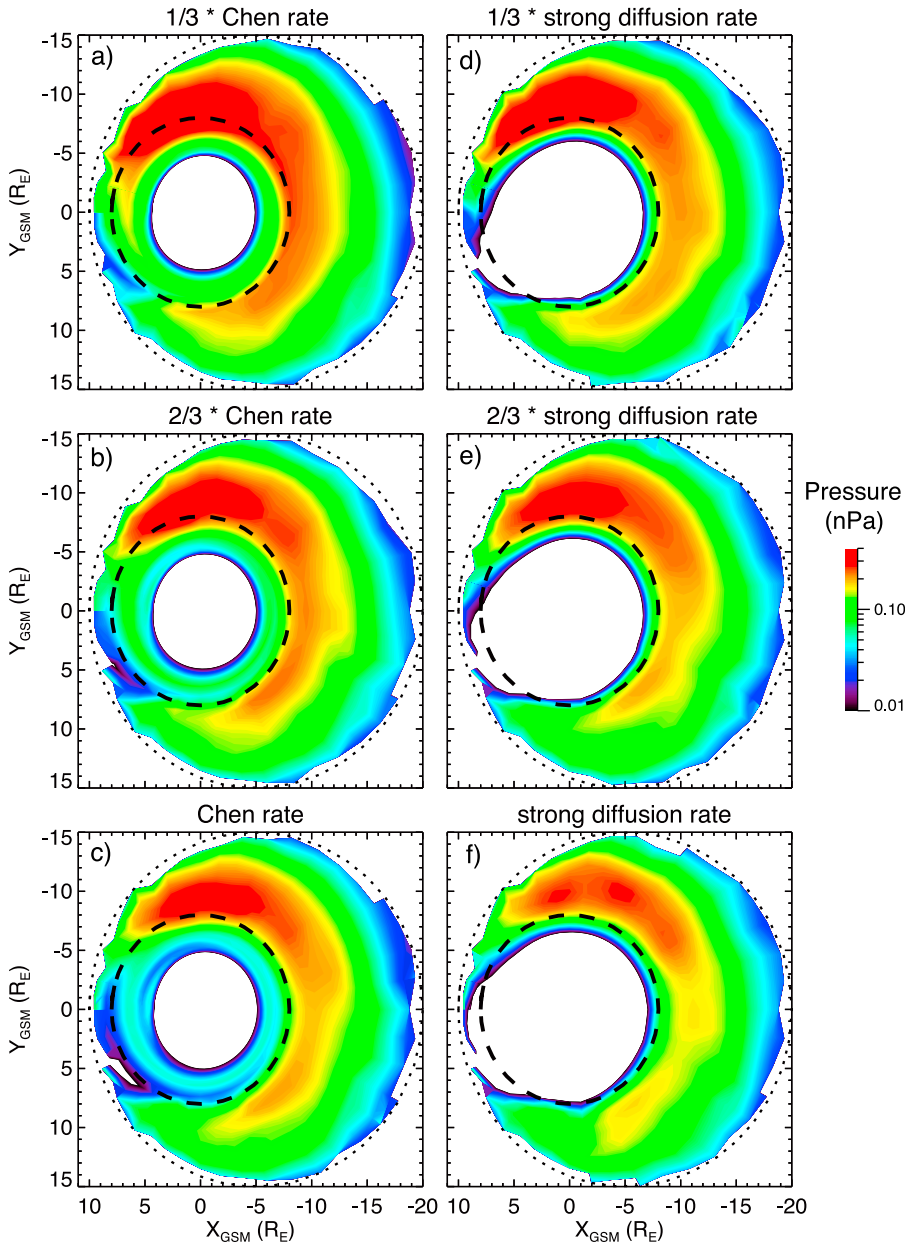

Figure 3. Electron pressures for the runs using (a) 1/3 of Chen loss rate, (b) 2/3 of Chen loss rate, (c) Chen loss rate, (d) 1/3 of strong diffusion everywhere loss rate, (e) 2/3 of strong diffusion everywhere loss rate, and (f) strong diffusion loss rate everywhere. The bold dashed black line in all plots is a circle with geocentric radius of 8 R_E.

inner magnetosphere can be also seen in the observations, indicating the Chen rate provides a more realistic electron loss in the inner magnetosphere. The above comparison shows the importance of realistic electron loss for modeling electron radiation belts since this high-energy electron population is the seed particles for the radiation belts. Note that the above comparison is only qualitative since the initial electron distribution used in this simulation to describe the trapped electrons in the inner magnetosphere is not empirical. It was simply obtained by driving particles earthward from the empirical tail boundary sources under 100 kV for 24 h to populate particles in the inner magnetosphere. This simple initial condition leads to a quantitative discrepancy between the observed and simulated differential fluxes in the inner magnetosphere.

4.2. Effect of MLT Dependent Loss Rates on Electron Precipitation to the Ionosphere

[23] Next, we examine the effect of MLT dependent loss rates on the precipitating plasma sheet electrons, which are known to be the main cause of diffuse aurora. More specifically, we focus on the effect on the precipitating electron energy fluxes and the Pedersen conductance they produce.

4.2.1. Energy Flux

[24] Figure 6 shows ionospheric plots of the precipitating electron energy flux computed from (3) for all the six loss

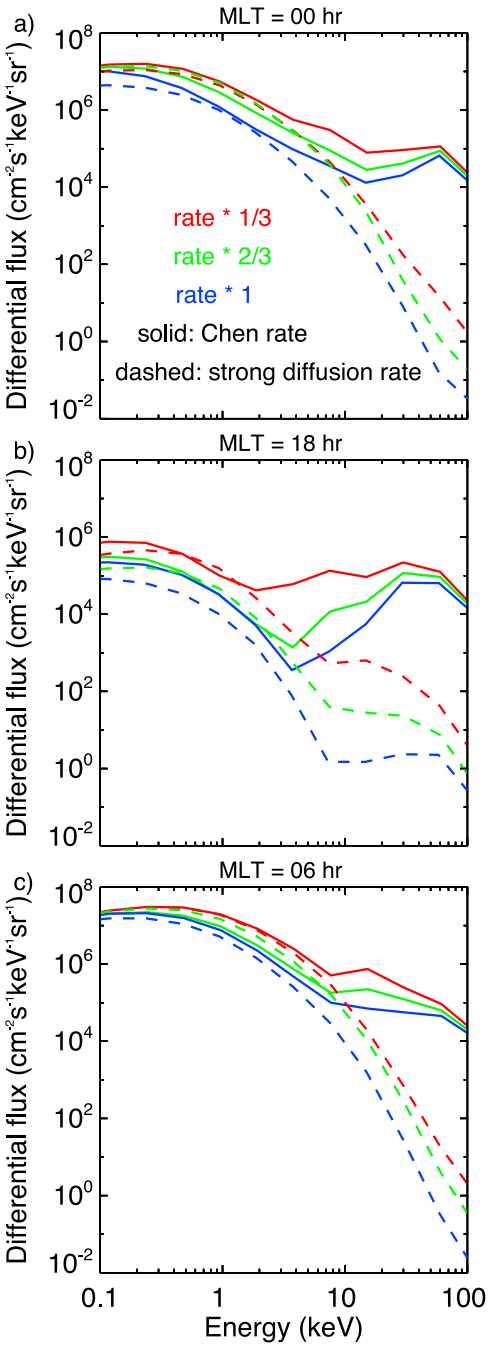

Figure 4. Electron energy spectra at geosynchronous at (top) midnight, (middle) dusk, and (bottom) dawn, for strong diffusion rate and its fractions cases with dashed lines, and for Chen rate and its fractions cases with solid lines (fraction of 1/3 with red, 2/3 with green, 1 with blue).

rate cases, with runs under the Chen rate and its fractions on the left, and runs under the strong diffusion rate and its fractions on the right. We can notice (i) a clear difference in the azimuthal distribution of the energy flux between the two major groups, with more significant enhancement in the premidnight energy fluxes in the strong diffusion everywhere cases than in the Chen rate cases, and (ii) that as the fraction increases (from Figures 6a to 6c or from Figures 6d to 6f), the overall energy flux increases, for both the major groups.

[25] As indicated by equations (2) and (6), the number of electrons precipitating is determined by the loss rate and the number of electrons in the plasma sheet, while the number of particles in the plasma sheet is determined by how many electrons have been lost as they drift from the outer boundary, which, as shown in equation (2), depends on the same loss rate. Combining equations (2), (5), and (6) we can estimate the number of precipitating electrons under a given loss rate (η_p) relative to the number of precipitating electrons under strong diffusion everywhere ($\eta_{p,strong}$) as electrons drifting from the same boundary sources,

$$\frac{\eta_{p,strong}}{\eta_p} = \frac{1}{factor}\exp\left[\int -dt \cdot (1/\tau(t)) \cdot (1 - factor(t))\right]$$

where τ is the lifetime of strong diffusion given by (7), *factor* is as defined in equation (6). Note that $factor \leq 1$. Therefore, η_p is expected to be smaller than $\eta_{p,strong}$ for timescales shorter than $-[\ln(factor)/(1 - factor)] \cdot \tau$. For example, for a factor of 1/3 and τ = 200 min for typical thermal plasma sheet electrons (see Figure 2), as electrons drift earthward from the tail boundary, η_p will be smaller than $\eta_{p,strong}$ within ~5 h, which is long enough for these electrons to occupy the region of the plasma sheet.

[26] The above estimate can explain why (i) the precipitating energy flux is enhanced in the premidnight sector in the strong diffusion everywhere cases compared to the Chen rate ones, even though the electron plasma sheet pressure is smaller in that region and (ii) the larger the fraction of a rate the more enhanced the energy flux, even though, again, the electron plasma sheet pressure is smaller.

[27] We next compare our results with the statistical DMSP electron diffuse aurora. The data set and methodology to construct the DMSP diffuse electron map is described in more details in the companion paper (S. Wing et al., Auroral particle precipitation characterized by the substorm cycle, submitted to *Journal of Geophysical Research*, 2012). Briefly, we used data obtained from SSJ4 and SSJ5 particle detectors on board of DMSP series satellites 1996–2007. We removed monoenergetic and wave or broadband acceleration events from the data set. The remaining events are defined as diffuse aurora. For substorm identifications, we used substorm onsets identified by *Liou et al.* [2001] and *Frey et al.* [2004]. The substorms in both of these substorm databases were identified from optical images obtained from Polar UVI [*Liou et al.*, 2001] and IMAGE FUV [*Frey et al.*, 2004] instruments. There are a total of 4681 events in the combined data sets. From this data set, we selected a total of 2464 isolated substorm events, that is, those that are separated by at least 5 h from other substorms. Then, we bin the DMSP electron spectra in 48 MLT bins by 40 MLAT bins by 16 time step bins. The time step is 15 min, so that analysis begins 120 min before onset and extends to 180 min after. The MLAT range is 50–90°, with data from the two hemispheres combined. Thus, although the identification of a substorm onset is nearly all from the northern hemisphere global images, the particle precipitation maps contain equal amounts of northern and southern hemisphere data. Then the time of each spectral observation at 1 s resolution is compared with the list of substorm onsets. If the particle observation is

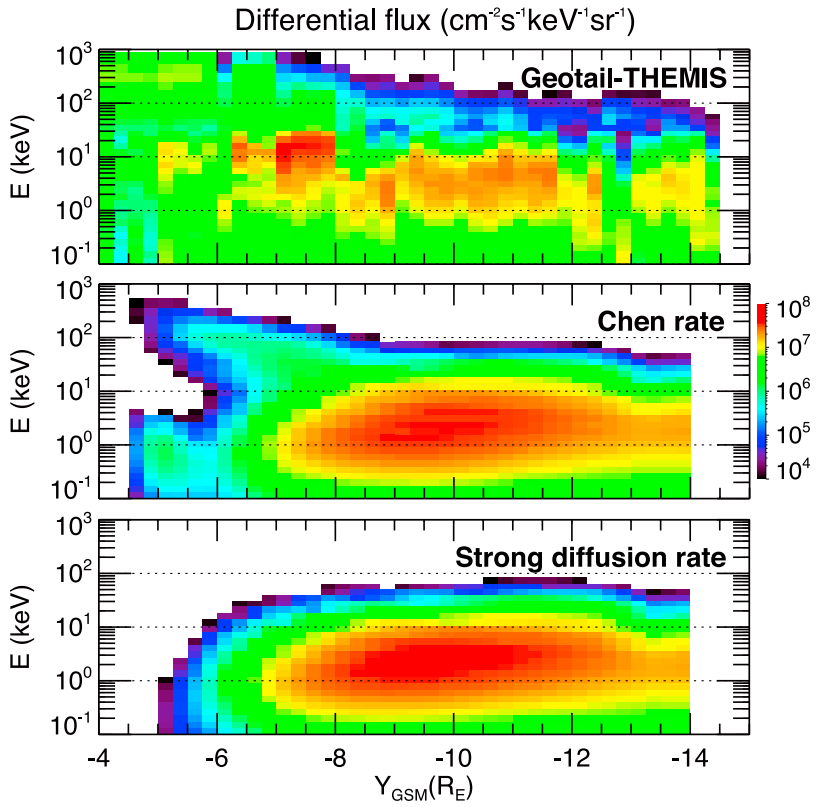

Figure 5. Electron energy spectra along the dawn meridian for the (bottom) strong diffusion everywhere loss rate case (middle) and Chen loss rate case, and (top) observed electron energy spectra taken from Figure 10 of *Wang et al.* [2011].

within 120 min before onset and 180 min after onset, it is added to the appropriate bin (determined from MLAT, MLT, and time from onset).

[28] Figure 7 shows the median diffuse electron aurora energy fluxes at the interval within 15 min before the substorm onset. Note that our method is similar to the method used in *Newell et al.* [2010], except that they calculated the mean rather than the median. It turns out that the distribution of the electron energy flux is not Gaussian but rather with an extended tail of the high-energy fluxes [see, e.g., *Newell and Gjerloev*, 2011]. Therefore, the median would better characterize a typical substorm than the mean, which would be biased toward stronger substorms.

[29] It can be seen that, although in general our simulated fluxes have higher magnitudes than the observed ones, the Chen rate cases capture better features of the DMSP azimuthal distribution, in particular the fluxes being weaker in the premidnight than in the postmidnight sector. The strong diffusion everywhere cases have either too large duskside precipitation (the 2/3 of strong diffusion and strong diffusion everywhere cases) or a very symmetric premidnight – postmidnight (between 21 hr and 3 hr of MLT) distribution (1/3 of strong diffusion everywhere case). It can also be seen that the result of the 1/3 of Chen rate is closest to the observations. The better agreement with the Chen rate indicates that it is crucial to take into account the distributions of wave activity in order to prescribe the loss rate more realistically. This improvement is also quite encouraging considering the simplicity of the Chen rate. However, the fact that our simulation results are almost a factor of two larger than the observational ones can probably be attributed to our loss rates being independent of geomagnetic activity, while the DMSP precipitating electron fluxes shown in Figure 7 are only during substorm growth phase. Since the magnitude and spatial distribution of waves vary with geomagnetic activity, in would be beneficial to develop a loss rate to be developed parameterized with geomagnetic activity in the future. Our results are consistent with previous results by *Chen et al.* [2005]. They also found that by using an MLT dependent, less than everywhere strong diffusion scattering rate, the azimuthal distribution of their simulated precipitating energy flux was in better agreement with observed diffuse aurora, inferred by NOAA-12 data and Polar/UVI images. Note that our simulated energy fluxes are located ~2°–5° poleward of the observed ones, which is mainly due to the limitation of field line stretching of our magnetic field model (see discussion in section 2.1).

4.2.2. Conductance

[30] In Figure 8, similar to Figure 6, we show Pedersen conductance computed from (7) for all the six loss rate cases. Note that we have also plotted the background Solar-EUV-generated conductance. We see azimuthal distributions that are similar to those for the energy fluxes discussed above, as expected since the Pedersen conductance is proportional to the square root of the precipitating energy flux. There is higher conductance in the postmidnight sector as well as a pronounced peak in the premidnight sector for the strong

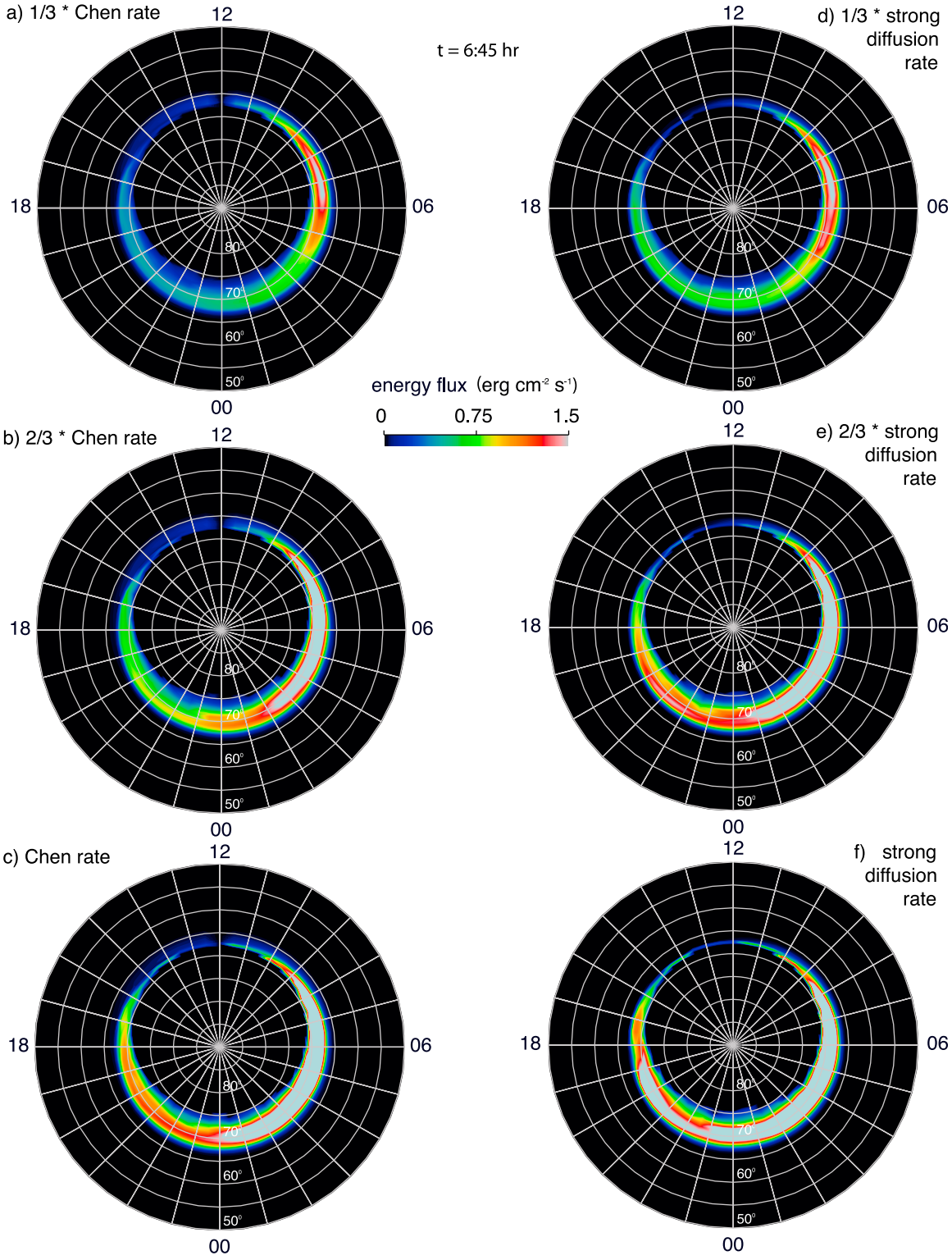

Figure 6. Ionospheric plots of the precipitating electron energy flux for the runs using (a) 1/3 of Chen loss rate, (b) 2/3 of Chen loss rate, (c) Chen loss rate, (d) 1/3 of strong diffusion everywhere loss rate, (e) 2/3 of strong diffusion everywhere loss rate, and (f) strong diffusion loss rate everywhere.

diffusion everywhere cases, while the Chen rate cases have a more pronounced dawn-dusk asymmetry with their conductivities in the premidnight sector weaker than those in the postmidnight sector.

4.3. Effect of Loss Rates on M-I Coupling

[31] In the previous section we showed how different electron loss rates affect the electron precipitation to the

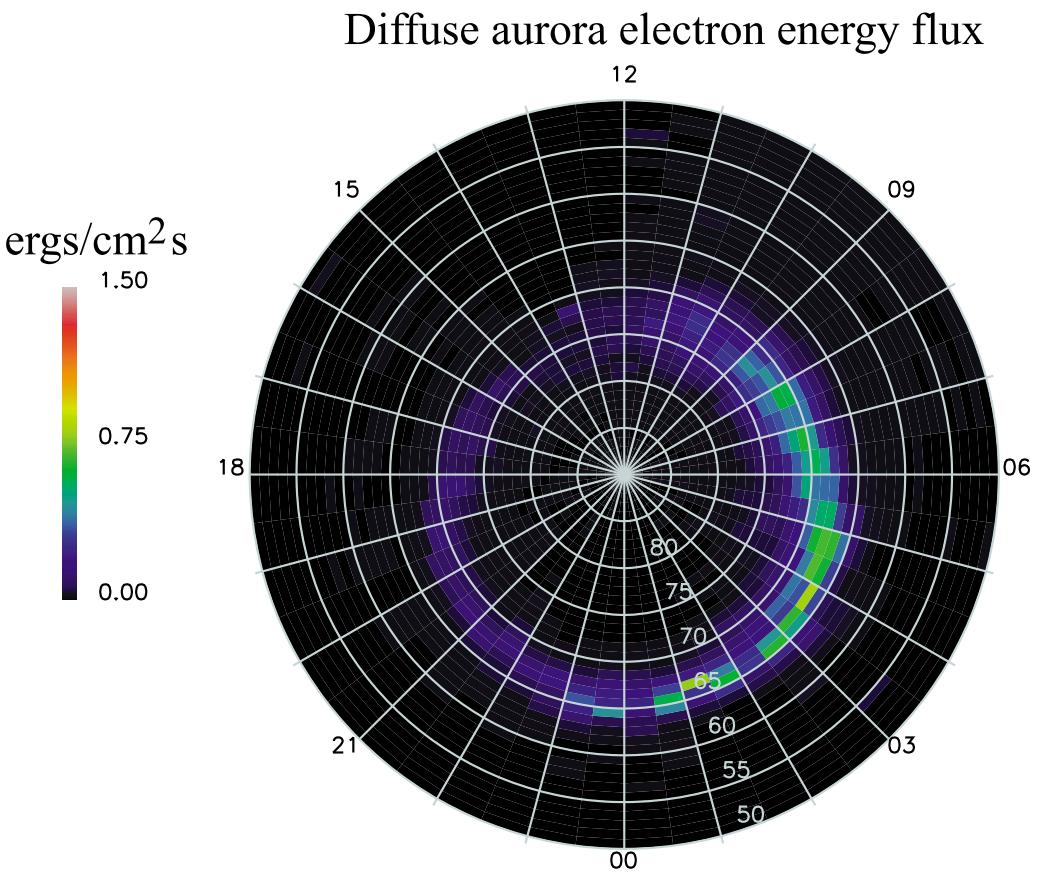

Figure 7. Statistical DMSP data of median electron energy fluxes 15 min before the substorm onset.

ionosphere and the resulting ionospheric Pedersen conductance. In this section we investigate the effect of the different electron loss rates on the M-I coupling, with a focus on the penetration of the plasma sheet into the inner magnetosphere, since the shielding of the penetration strongly depends on the ionospheric conductivity [e.g., *Gkioulidou et al.*, 2011].

[32] For this part of the study we conducted two different runs, one with the strong diffusion everywhere electron loss rate and the other one with the Chen electron loss rate. For both runs, $\Delta\Phi_{PC}$ of 40 kV is kept constant for 5 simulation hours (t = 5 h), and we then increase it sharply to 90 kV within 10 min and keep it constant for another 10 min (t = 5:20 h). We chose this sharp and large increase of the $\Delta\Phi_{PC}$, which is more representative of storm time convection enhancement than a substorm growth phase, because the shielding development is easier to evaluate by keeping the convection steady after it has been substantially enhanced.

[33] In Figure 9 we show the Pedersen conductance together with equipotential contour lines within the ionosphere at t = 5:20 h for the Chen loss rate case (Figure 9, top) and the strong diffusion rate case (Figure 9, bottom). We see that the shielding of the convection electric field has started developing for both cases (notice the bending of the equipotential contour lines at lower latitudes). We can see that, although above 68° latitude, the conductance in the strong diffusion everywhere case is stronger than in the Chen rate case, below 68° latitude, there is a sharp decrease in the conductance in the strong diffusion everywhere case, while the decrease in the Chen rate case is smoother at all nightside MLTs. Especially at the postmidnight MLTs (0–4 h), the conductance in the Chen rate case below 65° is ~2 ohms^{-1} and it extends to as low as ~63°, while conductance drops to almost zero below 65° for the strong diffusion everywhere case. Although the precipitating energy flux is larger in the plasma sheet region, this more abrupt conductance decrease from higher to lower latitudes in the strong diffusion everywhere case is due to the electron population that contributes to the conductance getting lost rapidly due to very short lifetimes inside 6 R_E. For the Chen rate case, the lifetimes increase significantly with decreasing distance, allowing the electrons in the closed drift path region to remain there for a longer time (see discussion in section 4.1) and produce conductance.

[34] At this point we should remind the readers that the conductance calculation of *Robinson et al.* [1987] is based on the assumption of a single Maxwellian electron energy distribution. However, the spectrum of simulated precipitating electrons near the edge of the plasma sheet is not very well approximated with a single-Maxwellian. In fact, our distribution function often includes two components: a low-energy component that might contribute significantly to the number flux but not the energy flux, and a high-energy component (tens of keV) that might contribute significantly to the energy flux but not to the number flux. We have done a more careful analysis of a sample of 12 nightside grid points using two-Maxwellian distributions that fit the RCM spectra considerably better than single-Maxwellians. We found that the single-Maxwellians nearly always underestimate the

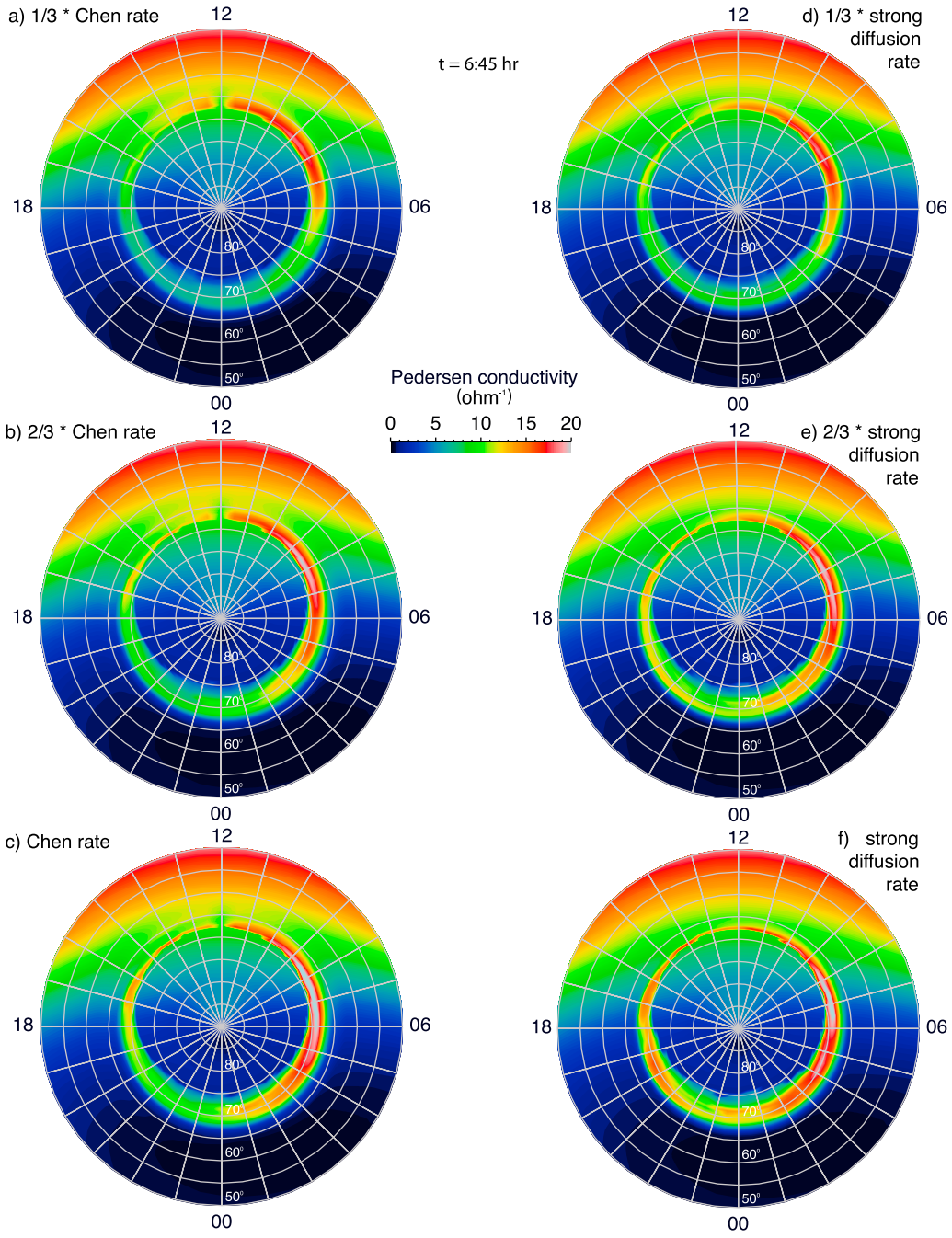

Figure 8. Ionospheric plots of the Pedersen conductance for the runs using (a) 1/3 of Chen loss rate, (b) 2/3 of Chen loss rate, (c) Chen loss rate, (d) 1/3 of strong diffusion everywhere loss rate, (e) 2/3 of strong diffusion everywhere loss rate, and (f) strong diffusion loss rate everywhere.

high-energy tail of the distribution leading typically to an underestimate of the ratio of Hall to Pedersen conductance. More specifically, the root mean square error from using the single-Maxwellian fit indicates an overestimate of 12% in Pedersen conductance and an underestimate of 32% in Hall conductance. Nonetheless, for this study we calculated the conductances under the assumption of a single-Maxwellian distribution.

[35] The relatively lower conductance at lower latitudes in the strong diffusion everywhere case leads to stronger shielding of the convection electric field in that region, as indicated by the sharper bending of the equipotentials. The different shielding development at different latitudes for the two cases can be seen more clearly in Figure 10a where we have plotted the latitudinal profile of the azimuthal component of the electric field (the negative azimuthal electric field gives equatorward flow in the ionosphere and earthward flow in the equatorial plasma sheet) at MLT = 21 h for the Chen rate case (blue curves) and the strong diffusion rate case (red curves), at t = 5:10 h (just after reaching $\Delta\Phi_{PC}$ = 90 kV, dashed lines) and t = 5:20 h (90 kV for 10 min, solid lines). We see that from 5:10 to 5:20, at higher (lower)

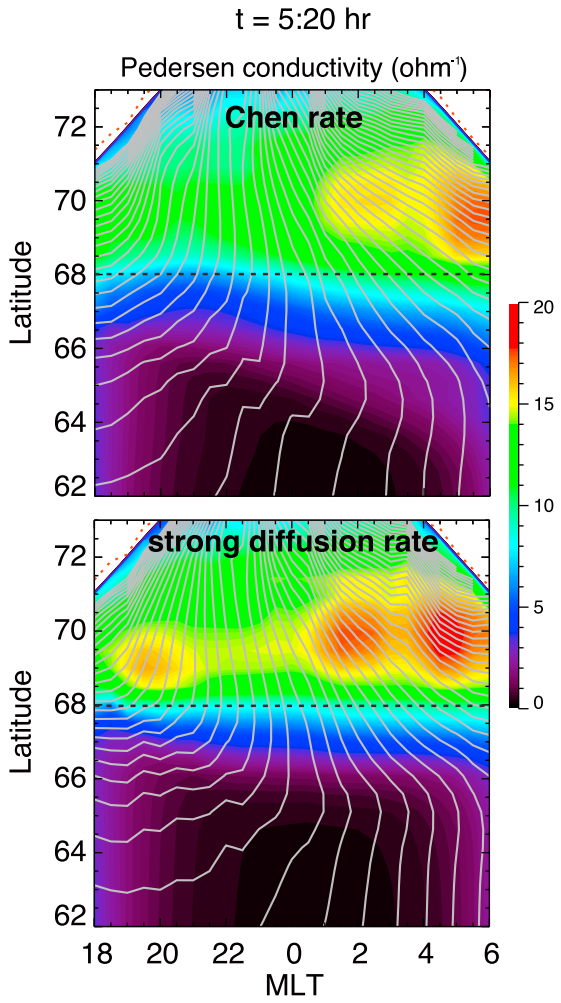

Figure 9. Pedersen conductance and equipotential contour lines of 0.5 kV interval, at t = 5:20 h, for (top) the Chen loss rate case and (bottom) the strong diffusion rate case. Black dotted line indicates 68° latitude.

latitudes, above 66° (below 65°), in the strong diffusion everywhere case, where the conductance is higher (lower) than in the Chen rate one, the electric field magnitude decreases less (more), which means that the shielding development is slower (faster).

[36] The azimuthal component of the electric field is responsible for the penetration of the plasma sheet population into the inner magnetosphere. In Figure 10b we show the longitudinal ion pressure profiles at 5.5 R_E (this radial distance is chosen because it was earthward of the plasma sheet inward edge before the convection enhancement), at t = 5:20 h, for the Chen rate case (blue) and the strong diffusion rate case (red). The ion pressure is larger in the Chen rate case than in the strong diffusion rate case, which is due to the protons penetrating further earthward in the Chen rate case due to slower shielding development at lower latitudes. On the other hand, in Figure 10c we have plotted the same pressure profiles at 8 R_E (this radial distance was already within the plasma sheet before the convection enhancement), which corresponds to higher latitudes, and, as it can be seen, the ion pressure is higher for the strong diffusion everywhere case in that region. This is due to larger energization of

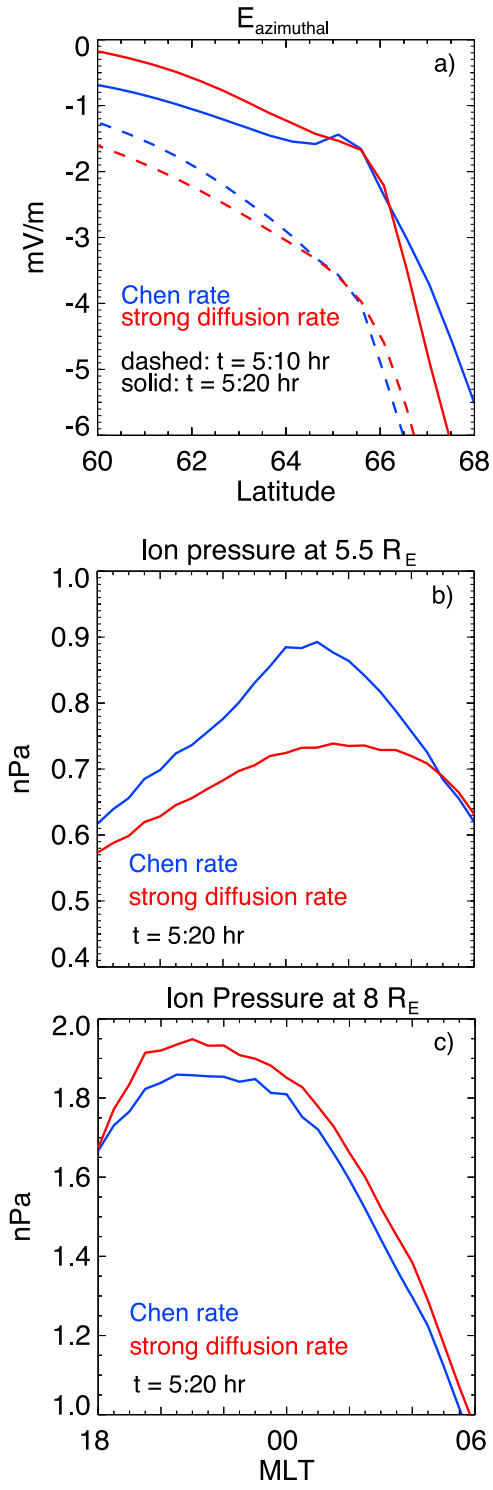

Figure 10. (a) Latitudinal profile of the azimuthal component of the electric field at MLT = 21 h for the Chen rate case (blue curves) and the strong diffusion rate case (red curves), at t = 5:10 h and t = 5:20 h, (b) longitudinal ion pressure profiles at 5.5 R_E at t = 5:20 h, for the Chen rate case (blue), and the strong diffusion rate case (red), and (c) same as Figure 10b but at 8 R_E.

protons by the stronger electric field because of the less efficient shielding development in the strong diffusion everywhere case.

5. Summary and Conclusions

[37] We have used simulation results to evaluate the effects of a more realistic and wave-activity based MLT dependent electron loss rate (the Chen rate), in comparison with strong diffusion loss rate everywhere, on the plasma sheet ions and electrons, their coupling with the ionosphere, and their penetration into the inner magnetosphere. We simulate the earthward transport of ions and electrons from observationally based tail sources under self-consistent electric and magnetic field using the RCM coupled with a modified Dungey force-balanced magnetic field model. In addition, we also evaluate the effects as the Chen rate and strong diffusion rate everywhere decrease by factors of 2/3 and 1/3 to take into account the variation of the loss rates corresponding to different geomagnetic activity, as suggested by observations.

[38] In the first part of our paper we evaluated the effect of the different loss rates on the plasma sheet and inner magnetosphere electron population, as well as energy fluxes of electrons precipitating into the ionosphere and as a result, on ionospheric Pedersen conductance. Our results focused on substorm growth phase convection enhancement so that they can be compared more appropriately with observations.

[39] We found that the electron pressures of the Chen rate cases are larger than those of the strong diffusion everywhere cases in the premidnight sector, since, beyond $r_0 \sim 8$ R_E, the Chen lifetimes for higher energy electrons are much larger than the lifetime of strong diffusion everywhere at dusk. The lifetime of the Chen rate becomes significantly smaller than the strong diffusion lifetime with decreasing radial distance inside $r \sim 7$ $R_{E,}$ allowing the electrons penetrating to the inner magnetosphere to remain there for many hours or more under the Chen rate, while the electrons get lost within minutes under strong diffusion. The simulated electron energy spectra in the inner magnetosphere under the Chen rate can qualitatively account for the 20–200 keV ring current electrons observed by THEMIS, but the same is not true for the strong-diffusion case. Therefore a more realistic loss rate is important for these high-energy electrons in the inner magnetosphere, and thus also for understanding the radiation belts since they are the seed population for the radiation belts.

[40] Precipitating electron energy fluxes, and their resulting Pedersen conductivities in the ionosphere are found to be significantly enhanced at premidnight MLTs in the strong diffusion everywhere cases but not in the Chen rate cases. The dawn-dusk asymmetric profile of the precipitating energy fluxes in the Chen rate cases, with much higher energy flux at dawn rather than at dusk, agrees better with statistical DMSP observations compared to the asymmetry of the strong diffusion everywhere cases.

[41] In the second part of our paper, since we have established that using the more realistic Chen electron loss rate results in electron properties that are closer to the observed ones in both the ionosphere and magnetosphere than does the strong diffusion one, we investigated the effect of the different loss rates on the shielding of the convection electric field via ionospheric Pedersen conductance. For this purpose, we focused on storm-like convection enhancement, for which the shielding development is more distinct.

[42] We found that although at higher latitudes the conductance in the strong diffusion everywhere case is stronger than in the Chen rate case, at lower latitudes there is a sharp decrease in the conductance in the strong diffusion everywhere case. That sharp decrease is attributed to the high-energy electron population, responsible for the conductance, being lost more rapidly due to lifetimes becoming very short inside 6 R_E for the strong diffusion everywhere rate. On the other hand, the Chen rate case includes weak pitch-angle scattering at lower L values, allowing the electrons within the closed drift path region to remain there for a longer time and produce conductance. This results in conductance that extends further equatorward at all nightside MLTs. Therefore, the relatively higher conductance at lower latitudes in the Chen rate case leads to less efficient shielding of the enhanced convection electric field, allowing for further inward penetration of the proton plasma sheet into the inner magnetosphere, compared to the strong diffusion everywhere case.

[43] **Acknowledgments.** The work by Matina Gkioulidou has been supported by NASA grant NNX09AQ41H and NSF grant ATM-0819864. The work by C.-P. Wang and L. R. Lyons has been supported by NASA grants NNX11AJ12G and NNX07AG42G, and NSF grant ATM-0819864. The work by Simon Wing has been supported by NSF grants ATM-0802715 and AGS-1058456. The work by R. A. Wolf has been supported by NASA grant NNX10AQ43G. The work by Tung-Shin Hsu has been supported by NSF Space Weather grant AGS-0720422 and NSF-GEM grant AGS-1003854. The authors would like to thank Mike Schulz and Margaret Chen for very useful discussions.

[44] Robert Lysak thanks the reviewers for their assistance in evaluating the paper.

References

Albert, J. M. (1994), Quasi-linear pitch angle diffusion coefficients: Retaining high harmonics, *J. Geophys. Res.*, *99*, 23,741–23,745, doi:10.1029/94JA02345.

Anderson, P. C., D. L. McKenzie, M. J. Brittnacher, M. W. Chen, M. Hairston, and M. F. Thomsen (2000), Global storm time auroral X-ray morphology and timing and comparison with UV measurements, *J. Geophys. Res.*, *105*, 15,757–15,777, doi:10.1029/1999JA000355.

Ashour-Abdalla, M., and C. F. Kennel (1978), Diffuse auroral precipitation, *J. Geomagn. Geoelectr.*, *30*, 239–255, doi:10.5636/jgg.30.239.

Chen, M. W., and M. Schulz (2001), Simulations of diffuse aurora with plasma sheet electrons in pitch angle diffusion less than everywhere strong, *J. Geophys. Res.*, *106*(A12), 28,949–28,966, doi:10.1029/2001JA000138.

Chen, M. W., M. Schulz, P. C. Anderson, G. Lu, G. Germany, and M. Wüest (2005), Storm time distributions of diffuse auroral electron energy and X-ray flux: Comparison of drift-loss simulations with observations, *J. Geophys. Res.*, *110*, A03210, doi:10.1029/2004JA010725.

Dungey, J. W. (1963), The structure of the exosphere or adventures in velocity space, in *Geophysics, The Earth's Environment*, edited by C. DeWitt, J. Hieblot, and A. Lebeau, pp. 503–550, Gordon and Breach, London.

Ebihara, Y., and M.-C. Fok (2004), Postmidnight storm-time enhancement of tens-of-keV proton flux, *J. Geophys. Res.*, *109*, A12209, doi:10.1029/2004JA010523.

Frey, H. U., S. B. Mende, V. Angelopoulos, and E. F. Donovan (2004), Substorm onset observations by IMAGE-FUV, *J. Geophys. Res.*, *109*, A10304, doi:10.1029/2004JA010607.

Gkioulidou, M., C.-P. Wang, L. R. Lyons, and R. A. Wolf (2009), Formation of the Harang reversal and its dependence on plasma sheet conditions: Rice convection model simulations, *J. Geophys. Res.*, *114*, A07204, doi:10.1029/2008JA013955.

Gkioulidou, M., C.-P. Wang, and L. R. Lyons (2011), Effect of self-consistent magnetic field on plasma sheet penetration to the inner magnetosphere: Rice convection model simulations combined with modified Dungey force-balanced magnetic field solver, *J. Geophys. Res.*, *116*, A12213, doi:10.1029/2011JA016810.

Hardy, D., M. Gussenhoven, and E. Holeman (1985), A statistical model of auroral electron precipitation, *J. Geophys. Res.*, *90*(A5), 4229–4248, doi:10.1029/JA090iA05p04229.

Hardy, D. A., M. S. Gussenhoven, R. Raistrick, and W. J. McNeil (1987), Statistical and functional representations of the pattern of auroral energy flux, number flux, and conductivity, *J. Geophys. Res.*, *92*, 12,275–12,294, doi:10.1029/JA092iA11p12275.

Hsu, T.-S., and R. L. McPherron (2012), A statistical analysis of substorm associated tail activity, *Adv. Space Res.*, *50*(10), 1317–1343, doi:10.1016/j.asr.2012.06.034.

Johnstone, A. D., D. M. Walton, R. Liu, and D. A. Hardy (1993), Pitch angle diffusion of low-energy electrons by whistler mode waves, *J. Geophys. Res.*, *98*, 5959–5967, doi:10.1029/92JA02376.

Kennel, C. F., and M. Ashour-Abdalla (1982), Electrostatic waves and the strong diffusion of magnetospheric electrons, in *Magnetospheric Plasma Physics*, edited by A. Nishida, pp. 245–344, Cent. Acad. Publ., Tokyo, doi:10.1007/978-94-009-7743-3_5.

Kennel, C. F., F. L. Scarf, R. W. Fredricks, J. H. McGehee, and F. V. Coroniti (1970), VLF electric field observations in the magnetosphere, *J. Geophys. Res.*, *75*, 6136–6152, doi:10.1029/JA075i031p06136.

Koons, H. C., and J. L. Roeder (1990), A survey of equatorial magnetospheric wave activity between 5 and 8 R_E, *Planet. Space Sci.*, *38*, 1335–1341, doi:10.1016/0032-0633(90)90136-E.

Liou, K., P. T. Newell, D. G. Sibeck, C.-I. Meng, M. Brittnacher, and G. Parks (2001), Observation of IMF and seasonal effects in the location of auroral substorm onset, *J. Geophys. Res.*, *106*, 5799–5810, doi:10.1029/2000JA003001.

Liu, S., M. W. Chen, M. Schulz, and L. R. Lyons (2006), Initial simulation results of storm-time ring current in a self- consistent magnetic field model, *J. Geophys. Res.*, *111*, A04225, doi:10.1029/2005JA011194.

Lyons, L. R. (1974), Electron diffusion driven by magnetospheric electrostatic waves, *J. Geophys. Res.*, *79*, 575–580, doi:10.1029/JA079i004p00575.

Meredith, N. P., A. D. Johnstone, S. Szita, R. B. Horne, and R. R. Anderson (1999), "Pancake" electron distributions in the outer radiation belts, *J. Geophys. Res.*, *104*, 12,431–12,444, doi:10.1029/1998JA900083.

Newell, P. T., and J. W. Gjerloev (2011), Substorm and magnetosphere characteristic scales inferred from the SuperMAG auroral electrojet indices, *J. Geophys. Res.*, *116*, A12232, doi:10.1029/2011JA016936.

Newell, P. T., A. R. Lee, K. Liou, S.-I. Ohtani, T. Sotirelis, and S. Wing (2010), Substorm cycle dependence of various types of aurora, *J. Geophys. Res.*, *115*, A09226, doi:10.1029/2010JA015331.

Ni, B., R. M. Thorne, R. B. Horne, N. P. Meredith, Y. Y. Shprits, L. Chen, and W. Li (2011a), Resonant scattering of plasma sheet electrons leading to diffuse auroral precipitation: 1. Evaluation for electrostatic electron cyclotron harmonic waves, *J. Geophys. Res.*, *116*, A04218, doi:10.1029/2010JA016232.

Ni, B., R. M. Thorne, N. P. Meredith, R. B. Horne, and Y. Y. Shprits (2011b), Resonant scattering of plasma sheet electrons leading to diffuse auroral precipitation: 2. Evaluation for whistler mode chorus waves, *J. Geophys. Res.*, *116*, A04219, doi:10.1029/2010JA016233.

Roberts, C. S. (1969), Pitch angle diffusion of electrons in the magnetosphere, *Rev. Geophys.*, *7*, 305–337, doi:10.1029/RG007i001p00305.

Robinson, R. M., R. R. Vondrak, K. Miller, T. Dabbs, and D. Hardy (1987), On calculating ionospheric conductances from the flux and energy of precipitating electrons, *J. Geophys. Res.*, *92*, 2565–2569, doi:10.1029/JA092iA03p02565.

Schulz, M. (1974), Particle saturation of the outer zone: A nonlinear model, *Astrophys. Space Sci.*, *29*, 233–242, doi:10.1007/BF00642726.

Schulz, M., and M. Chen (2008), Field-line (Euler-potential) model of the ring current, 327, *J. Atmos. Sol. Terr. Phys.*, *70*, 482–489, doi:10.1016/j.jastp.2007.08.063.

Schumaker, T. L., M. S. Gussenhoven, D. A. Hardy, and R. L. Carovillano (1989), The relationship between diffuse auroral and plasma sheet electron distributions near local midnight, *J. Geophys. Res.*, *94*, 10,061–10,078, doi:10.1029/JA094iA08p10061.

Thorne, R. M., Y. Y. Shprits, N. P. Meredith, R. B. Horne, W. Li, and L. R. Lyons (2007), Refilling of the slot region between the inner and outer electron radiation belts during geomagnetic storms, *J. Geophys. Res.*, *112*, A06203, doi:10.1029/2006JA012176.

Toffoletto, F., S. Sazykin, R. Spiro, and R. Wolf (2003), Inner magnetospheric modeling with the Rice Convection Model, *Space Sci. Rev.*, *107*, 175–196, doi:10.1023/A:1025532008047.

Vasyliunas, V. M. (1970), Mathematical models of magnetospheric convections and its coupling to the ionosphere, in *Particles and Fields in the Magnetosphere*, edited by B. M. McCormac, pp. 60–71, D. Reidel, Hingham, Mass., doi:10.1007/978-94-010-3284-1_6.

Wang, C.-P., L. R. Lyons, T. Nagai, J. M. Weygand, and R. W. McEntire (2007), Sources, transport, and distributions of plasma sheet ions and electrons and dependences on interplanetary parameters under northward interplanetary magnetic field, *J. Geophys. Res.*, *112*, A10224, doi:10.1029/2007JA012522.

Wang, C.-P., M. Gkioulidou, L. R. Lyons, R. A. Wolf, V. Angelopoulos, T. Nagai, J. M. Weygand, and A. T. Y. Lui (2011), Spatial distributions of ions and electrons from the plasma sheet to the inner magnetosphere: Comparisons between THEMIS-Geotail statistical results and the Rice convection model, *J. Geophys. Res.*, *116*, A11216, doi:10.1029/2011JA016809.

Weimer, D. (1995), Models of high-latitude electric potentials derived with a least error fit of spherical harmonic coefficients, *J. Geophys. Res.*, *100*(A10), 19,595–19,607, doi:10.1029/95JA01755.